ADVANCES IN ATMOSPHERIC SCIENCES, VOL. 30, NO. 1, 2013, 175–192

Long-term Stability and Oceanic Mean State Simulated by the Coupled Model FGOALS-s2

LIN Pengfei*(林鹏飞), YU Yongqiang (俞永强), and LIU Hailong (刘海龙)

State Key Laboratory of Numerical Modeling for Atmospheric Sciences and Geophysical Fluid Dynamics, Institute of Atmospheric Physics, Chinese Academy of Sciences, Beijing 100029

(Received 28 February 2012; revised 8 April 2012)

ABSTRACT

We describe the long-term stability and mean climatology of oceanic circulations simulated by version 2 of the Flexible Global Ocean–Atmosphere–Land System model (FGOALS-s2). Driven by pre-industrial forcing, the integration of FGOALS-s2 was found to have remained stable, with no obvious climate drift over 600 model years. The linear trends of sea SST and sea surface salinity (SSS) were -0.04°C (100 yr)$^{-1}$ and 0.01 psu (100 yr)$^{-1}$, respectively.

The simulations of oceanic temperatures, wind-driven circulation and thermohaline circulation in FGOALS-s2 were found to be comparable with observations, and have been substantially improved over previous FGOALS-s versions (1.0 and 1.1). However, significant SST biases (exceeding 3°C) were found around strong western boundary currents, in the East China Sea, the Sea of Japan and the Barents Sea. Along the eastern coasts in the Pacific and Atlantic Ocean, a warm bias (>3°C) was mainly due to overestimation of net surface shortwave radiation and weak oceanic upwelling. The difference of SST biases in the North Atlantic and Pacific was partly due to the errors of meridional heat transport. For SSS, biases exceeding 1.5 psu were located in the Arctic Ocean and around the Gulf Stream. In the tropics, freshwater biases dominated and were mainly caused by the excess of precipitation. Regarding the vertical dimension, the maximal biases of temperature and salinity were located north of 65°N at depths of greater than 600 m, and their values exceeded 4°C and 2 psu, respectively.

Key words: FGOALS, stability, mean state, biases

Citation: Lin, P. F., Y. Q. Yu, and H. L. Liu, 2013: Long-term stability and oceanic mean state simulated by the coupled model FGOALS-s2. *Adv. Atmos. Sci.*, **30**(1), 175–192, doi: 10.1007/s00376-012-2042-7.

1. Introduction

Several generations of coupled models have been developed by Chinese scientists at State Key Laboratory of Numerical Modeling for Atmospheric Sciences and Geophysical Fluid Dynamics/Institute of Atmospheric Physics (LASG/IAP; Zhang et al., 1992; Chen et al., 1996; Chen et al., 1997a, b; Yu et al., 2002; Zhou et al., 2005), and have been widely applied in many fields of the geosciences. The latest coupled model is the Flexible Global Ocean–Atmosphere–Land System Model (FGOALS; Yu et al., 2004, 2007, 2011; Lin et al., 2011). FGOALS has four individual components – an atmosphere model, an ocean model, a sea ice model and a land model – that are coupled together by a flux coupler. Simulations from FGOALS have been cited by the Fourth Assessment Report of the Intergovernmental Panel on Climate Change (IPCC AR4).

To understand the causes of past climate change and project future climate change, it is necessary to evaluate the performance of coupled models in reproducing many aspects of past and modern climate. Firstly, the model should be integrated long-term (>1000 model years) without obvious drift when the external forcing is fixed. Secondly, the reliability of a coupled model should be evaluated on various timescales by analyzing the simulated climate mean features and patterns of periodic variability, such as intraseasonal oscillation (ISO), ENSO, Pacific Decadal Oscillation (PDO), and Atlantic Multidecadal Oscillation (AMO) .

The latest FGOALS has two parallel versions,

*Corresponding author: LIN Pengfei, linpf@mail.iap.ac.cn

FGOALS-s2 and FGOALS-g2, both of which contributed to the Couple Model Intercomparison Project Phase 5 (CMIP5). The primary difference between the versions is the adoption of different atmospheric models, i.e. the Spectral Atmospheric General Circulation Model of IAP LASG (SAMIL) and the Grid Atmospheric General Circulation Model of IAP LASG (GAMIL). Evaluation of version 1.0 of FGOALS-s (i.e. FGOALS-s1.0) has shown that the model performs well in reproducing irregular ENSO periods and East Asian monsoon; however, it does have the following major biases (Zhou et al., 2005). Excessively cold simulated temperatures in the NH lead to abnormally huge sea ice cover. The related Atlantic Meridional Overturning Circulation (AMOC) is very strong about 45 Sv (Zhou et al., 2005). In the SH, the SST is unnaturally warm, reducing sea ice extent (SIE). In the tropics, there is cold bias in the Indo-Pacific warm pool (bounded by a 28°C isotherm line). In the updated version of FGOALS-s1.0 (i.e. FGOALS-s1.1), the large cold bias about 2°C still exists, although the warm pool is improved (Bao et al., 2010; Zhang et al., 2010). The seasonal amplitude of simulated SST in the eastern equatorial Pacific is small and the phase is incorrect (Zhang et al., 2010). The amplitude of ENSO is smaller than its observed amplitude (Zhou et al., 2005). Moreover, the Antarctic Circumpolar Current (ACC) transport through the Drake Passage is weak (about 100–110 Sv, compared with an observed value of ∼135 Sv; Cunningham et al., 2003).

Only one version of FGOALS (FGOALS-g1.0) was included in the Coupled Model Intercomparison Project phase 3 (CMIP3), but three versions of FGOALS (gl, g2 and s2) are included in CMIP5. The basics of FGOALS-s2 and its components are briefly introduced by Bao et al. (2012).

The first purpose of the present paper is to describe the model stability and drift of FGOALS-s2 in long-term simulations. The second purpose is to evaluate the mean features of FGOALS from an oceanic perspective, comparing its simulations with observations and with the simulations from previous version, FGOAL-s1 (Zhou et al., 2005; Bao et al., 2010; Zhang et al., 2010). The improvements and simulated biases are highlighted, and the related causes and effects are briefly mentioned. The rest of the paper is organized as follows. Section 2 provides an overview of FGOALS and its individual components. The experiments and data used are also described in section 2. Section 3 examines the model stability and compares key oceanic variables of FGOALS-s2 with observations. Section 4 summarizes the improvement of FGOALS compared with its previous version, presents the biases and difference between FGOALS-s2 and other models, and suggests possible future modifications.

2. Model, experiments and data

2.1 *Model*

FGOALS-s2 and FGOALS-g2 differ in their adoption of different atmospheric models (i.e. SAMIL and GAMIL) and sea ice models, i.e. Community Sea Ice Model version 5 (CSIM5) and the updated Los Alamos sea ice model (CICE), respectively. In CMIP3, the Atmospheric General Circulation Model (AGCM) in FGOALS-g1.0 was GAMIL1.0. In the study, simulations of FGOALS-s2 were described and evaluated. The components and the model's performance have been briefly introduced by Bao et al. (2012). The oceanic component of FGOALS-s2 is the LASG/IAP Climate System Ocean Model version 2.0 (LICOM2.0). The remainder of this section introduces LICOM2.0 in detail.

LICOM was built and developed at LASG/IAP. The first LASG/IAP Oceanic General Circulation Model (OGCM) was developed in 1989 (Zhang and Liang, 1989) and has been developed successively since then. Working from the third generation OGCM (Jin et al., 1999), Liu et al. (2004a, b) built the fourth OGCM, named LICOM. LICOM is characterized by η-coordinates and a free surface. The mesoscale eddy parameterization of Gent and McWilliams (1990) was introduced into LICOM. LICOM2.0, an updated version of LICOM, has improved computing techniques, including increased computation precision and optimized parallel performance. Faulty restart processes have also been fixed in LICOM2.0.

Furthermore, LICOM2.0 has adjusted the horizontal and vertical resolution. The zonal resolution is 1°. The meridional resolution is 0.5° between 10°S and 10°N and increases gradually from 0.5° to 1° between 10°–20°N of latitude. Polarward of 20°, the meridional resolution is fixed to 1°. Such a meridional resolution setup can resolve effectively the equatorial waves. In order to better capture the upper mixed layer and thermocline, the vertical resolution in the upper 150 m has been adjusted to 10 m per layer (Wu et al., 2005). Below 150 m, there are 15 unevenly divided vertical layers. Besides the resolutions, LICOM2.0 has also been updated in terms of some key physical processes. The Richardson-number-dependent turbulent mixing scheme (Pacanowski and Philander, 1981) has been replaced by a second-order turbulent mixing scheme (Canuto et al., 2001, 2002). A solar radiation penetration scheme based on chlorophyll-a (Ohlmann, 2003) has been introduced (Lin et al., 2007). A shape-preserving advection scheme has been included (Xiao,

2006). The mesoscale eddy parameterization has been reasonably adjusted to obtain better simulation results, details of which can be found in Liu et al. (2012). It should be mentioned, however, that the shape-preserving and chlorophyll-a-based solar radiation schemes were not activated in the simulation experiments submitted to CMIP5. In the CMIP5 simulations, the atmosphere component is coupled with the ocean component through the coupler once per day in model time.

2.2 *Experiments and data*

To examine model stability, simulations from a preindustrial run were used. Before carrying out the preindustrial run, FGOALS-s2 was integrated for 1100 years using the present CO_2 concentration (fixed at 350 ppm) and starting from the annual mean observational sea temperature and salinity from the World Ocean Atlas 2005 (WOA05; Antonov et al., 2006; Locarnini et al., 2006). This experiment was called the "present climate run". Restarting from the initial value of the 1000th model year simulation fields in the present climate run, the preindustrial run was integrated by setting CO_2 concentration to its preindustrial level (fixed at 284 ppm), after which the experiment was run for another 1000 model years. This run was called the "preindustrial run". The simulations of the preindustrial run from the years 1251 to 1850 (total of 600 model years) were used for analysis in the present study. This is because the three initial values of historical runs forced by the scenarios of the Twentieth-Century Climate in Coupled Models (20C3M) project are chosen arbitrarily among the simulations of 600 model years from the preindustrial run.

Several variables, including the global-mean SST and sea surface salinity (SSS), global volume-mean ocean temperature and salinity (VOT, VOS), AMOC, ACC, SIE etc. were examined to test the model stability and possible drift. The historical runs were integrated over 156 model years using three different initial fields from the preindustrial run. Based on the simulations of three 20C3M runs, the ensemble means were used for comparison. Because the observational data are widely available after 1980, simulation data from historical runs forced by the exact CO_2 concentration after 1980 (from 1980 to 2005) were compared with observational data from the same periods where available. These observational data, related variables and references are listed in Table 1.

3. Results

3.1 *Long-term stability and drift*

Figure 1 shows time series of global-mean SST, global VOT and net heat flux at the sea surface. Over 600 model years, the global mean SST reached a quasi-equilibrium state with an extremely small decreasing trend of about 0.04°C (100 yr)$^{-1}$ (Table 2). The time-mean SST was about 17.3°C, colder than the observed value (∼18°C) from 1854 to 1859. The global

Table 1. The observed and reanalysis datasets used for comparison in the study.

Variables	Data set	Periods used	References
Sea surface temperature	ERSST v3b	1854–59; 1980–2005	Xue et al. (2003); Smith et al. (2008)
Ocean temperature and salinity	WOA05	Before 2005	Locarnini et al. (2006); Antonov et al. (2006)
Ocean temperature and salinity	PHC v3.0	Before 1998	Steele et al. (2001)
Heat fluxes	NOC 1.1a	1980–93	Grist and Josey (2003)
Rainfall	GPCP	1980–2005	Adler et al. (2003); Xie et al. (2003)
Evaporation	OAFLUX	1980–2005	Yu (2007); Yu et al. (2008)
Wind stress	ERA40	1958–2001	Uppala et al. (2005)
Sea ice extent	SMMR,ESMR, NIC, SSMI	1972–2002	Cavalieri and Parkinson (2003)
AMOC	RAPID	2004–09	Cunningham et al. (2007)
Meridional heat transport	WOCE	1990–2002	Ganachaud and Wunsch (2003)

Note: ERSST, Extended Reconstructed Sea Surface Temperature dataset; WOA05, World Ocean Atlas 2005; PHC, Polar science center Hydrographic Climatology; NOC, National Oceanography Centre; GPCP, Global Precipitation Climatology Project; OAFLUX, Objectively Analyzed Air–Sea Fluxes; ERA40, European Centre for Medium-Range Weather Forecasts (ECMWF) 40 Year Re-analysis; SMMR, the combined Nimbus 7 Scanning Multichannel Microwave Radiometer; ESMR, the Nimbus 5 Electrically Scanning Microwave Radiometer; NIC, National Ice Center; SSMI, Special Sensor Microwave Image; WOCE, World Ocean Circulation Experiment.

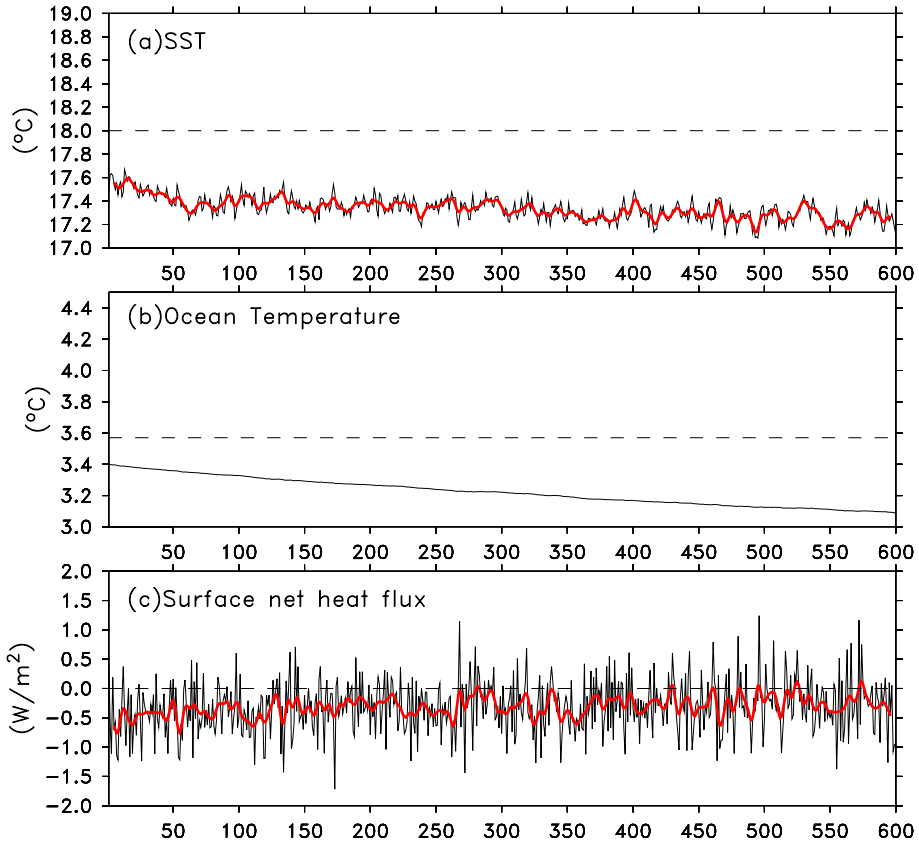

Fig. 1. 600-yr time series of (a) global mean SST (°C); (b) global volume-mean ocean temperature (°C); and (c) global mean net heat flux (W m^{-2}) at the sea surface in the preindustrial run simulated by FGOALS-s2. The net heat flux includes shortwave and longwave radiation, latent and sensible fluxes, and any heat exchange between ice/snow and the ocean. The black thin lines are annual mean values and the red thick lines are their 9-yr running mean values. The dashed lines in (a) and (b) are the observed values from ERSST3.0 from 1854–59 and WOA05, respectively.

VOT was also 0.15°C colder than the observed value in WOA05. The simulations of VOT showed a decreasing trend of about 0.05°C $(100\ yr)^{-1}$. The decreasing trend was due to the loss of net surface heat flux (∼0.32 W m^{-2}). To test the long-term behavior further, mean values and linear trends were calculated during the first 100-yr period and the last 100-yr period. The mean values for global SST and global VOT during the first 100-yr period were warmer than those during the last 100-yr period (Table 2), which was due to the loss of net heat flux (0.42 versus 0.24 W m^{-2}) at the sea surface during these two 100-yr periods. Furthermore, the loss was larger during the first 100-yr period (0.42 W m^{-2}) than in the last 100-yr period (0.24 W m^{-2}). The magnitudes of the trends decreased during the last 100-yr period, both for the global SST and for global VOT. This implies the model becomes more stable gradually as the time of integration increases.

The results of the time evolutions of global mean SSS, global VOS and net surface water fluxes are plotted in Fig. 2. The evolution of SSS reached a quasi-balance with a linear trend of 0.01 psu $(100\ yr)^{-1}$ and a mean value of about 34.49 psu during the 600-yr period. The mean value of SSS was 0.08 psu fresher than the observed value from WOA05. However, the global VOS had an increasing salty trend [∼0.01 psu $(100\ yr)^{-1}$] and was 0.21 psu saltier than the observed value. This was due to the loss ($\sim 2.6\times10^{-8}$ kg m^{-2} s^{-1}) of net water flux at the sea surface. The seawater became saltier during the last 100-yr period compared with the first 100-yr period. The linear trend for global SSS changed slightly in the last 100-yr period relative to the first 100-yr period. The linear trends of global VOS did not show any obvious change during these two periods.

To test the long-term behavior of the model at high latitudes, time series of SIEs in the NH and the SH were used. Due to the obvious seasonal variations of sea ice, the SIEs in March and September were chosen to examine long-term sea ice trends. The time evolu-

Table 2. The mean values and linear trends $(100\ \mathrm{yr})^{-1}$ of physical variables (calculated from Figs. 1–4) in the preindustrial run simulated by FGOALS-s2.

		OBS	FGOALS (1–600 yrs)	FGOALS (1–100 yrs)	FGOALS (501–600 yrs)
Global SST (°C)	Mean	18.0	17.34	17.43	17.27
	Trend		−0.04	−0.23	−0.04
Global ocean	Mean	3.57	3.22	3.36	3.11
temperature (°C)	Trend		−0.05	−0.07	−0.04
Global SSS (Psu)	Mean	34.57	34.49	34.47	34.51
	Trend		0.01	0.01	0.02
Global ocean salinity	Mean	34.72	34.93	34.90	34.96
(Psu)	Trend		0.01	0.01	0.01
Global net heat flux	Mean		−0.31	−0.42	−0.24
($\mathrm{W\ m^{-2}}$)	Trend				
Global net water flux	Mean		-2.63×10^{-8}	-4.68×10^{-8}	-1.66×10^{-8}
($\mathrm{kg\ m^{-2}\ s^{-1}}$)	Trend				
NH SIE in September	Mean	6.95	8.08	7.84	8.31
($10^6\ \mathrm{km^2}$)	Trend		0.09	0.77	−0.25
NH SIE in in March	Mean	15.40	13.45	13.32	13.54
($10^6\ \mathrm{km^2}$)	Trend		0.05	0.36	0.06
SH SIE in September	Mean	18.27	22.92	21.49	23.85
($10^6\ \mathrm{km^2}$)	Trend		0.47	0.51	1.28
SH SIE in March	Mean	4.03	7.53	7.28	7.74
($10^6\ \mathrm{km^2}$)	Trend		0.11	0.32	0.54
AMOC Strength (Sv)	Mean	18.5	20.00	20.33	19.62
	Trend		−0.18	−2.28	0.32
ACC at the Drake	Mean	134.5	143.7	142.9	143.6
Passage (Sv)	Trend		0.02	−1.55	−2.12

tions of SIEs in the NH and SH are plotted in Fig. 3. The SIEs were maintained at a stable value with a very small linear trend. In the NH, during a 600-yr period, the trends in SIEs were 0.05 $\times10^6$ km^2 $(100\ \mathrm{yr})^{-1}$ and 0.09 $\times10^6$ km^2 $(100\ \mathrm{yr})^{-1}$ in March and September, respectively. In the SH, the trend in SIEs in September was relatively large during a 600-yr period. The trends of SIEs were 0.11 $\times10^6$ km^2 $(100\ \mathrm{yr})^{-1}$ and 0.47×10^6 km^2 $(100\ \mathrm{yr})^{-1}$ in March and September, respectively. In the last 100-yr period in the NH, compared to the first 100-yr period, the trends decreased from 0.36×10^6 km^2 $(100\ \mathrm{yr})^{-1}$ to -0.061×10^6 km^2 $(100\ \mathrm{yr})^{-1}$ in March and from 0.77×10^6 km^2 (100 yr)$^{-1}$ to -0.25×10^6 km^2 $(100\ \mathrm{yr})^{-1}$ in September. In the SH, the trends increased from 0.32×10^6 km^2 (100 yr)$^{-1}$ to 0.54×10^6 km^2 $(100\ \mathrm{yr})^{-1}$ in March and from 0.51×10^6 km^2 $(100\ \mathrm{yr})^{-1}$ to 1.28×10^6 km^2 $(100\ \mathrm{yr})^{-1}$ in September. This implies the trend of SIEs in the SH is more pronounced than in the NH. Meanwhile, the trend of SIEs in the SH is more pronounced in September than in March.

In the NH, the mean SIEs were about 13.45×10^6 km^2 and 8.08×10^6 km^2 in March and September, respectively. These SIEs were comparable with observed values, i.e. 15.4×10^6 km^2 and 6.95×10^6 km^2, respectively (Cavalieri and Parkinson, 2003). Meanwhile, in the SH, the mean SIEs were about 7.53×10^6 km^2 and 22.92×10^6 km^2 in March and September, respectively, and the corresponding observed areas having been reported as 4.03×10^6 km^2 and 18.27×10^6 km^2, respectively (Cavalieri and Parkinson, 2003). The SIEs in the SH in March and September were larger than corresponding observed values.

Along with the evolutions of temperature, salinity and SIE in the NH and SH, the time evolutions of oceanic circulations such as AMOC and ACC were also examined (Fig. 4). The strength of AMOC averaged over 25°–35°N, 900–1200 m in depth, and the volume transport through the Drake Passage, were stable with a very small trend (Fig. 4). During the 600-yr period, the linear trends were −0.18 Sv $(100\ \mathrm{yr})^{-1}$ and 0.02 Sv $(100\ \mathrm{yr})^{-1}$, respectively. The linear trend of the strength of AMOC was −2.28 Sv $(100\ \mathrm{yr})^{-1}$ during the first 100-yr period and 0.32 Sv $(100\ \mathrm{yr})^{-1}$ during the last 100-yr period. These trends canceled each other out, and the overall trend during the 600-yr period was small. For ACC, although the linear trends were −1.55 Sv $(100\ \mathrm{yr})^{-1}$ and −2.12 Sv $(100\ \mathrm{yr})^{-1}$ during the first and last 100-yr periods, respectively, the linear trend over the total 600-yr period was small due to the positive trends in the period from 101–500 model years (not shown). The magnitudes of the simulated

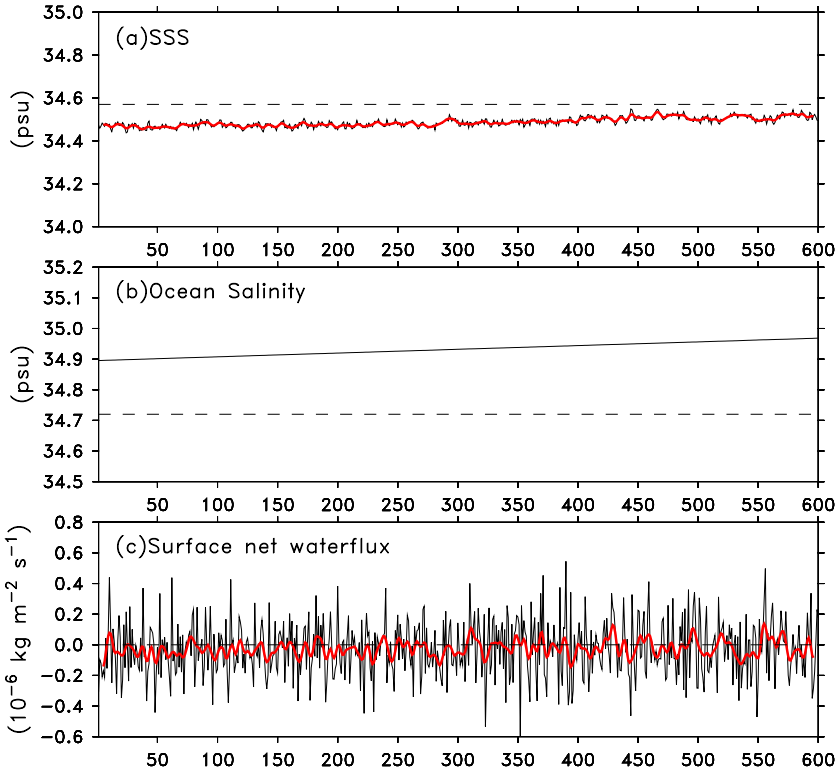

Fig. 2. 600-yr time series of (a) global mean SSS (psu); (b) global volume-mean ocean salinity (psu); and (c) global mean net water flux (10^{-6} kg m^{-2} s^{-1}) at the sea surface in the preindustrial run simulated by FGOALS-s2. The net water flux includes precipitation, evaporation, runoff, and snow/ice melt or formation. The black thin lines are annual mean values and the red thick lines are their 9-yr running mean values. The dashed lines in (a) and (b) are the observed values from WOA05.

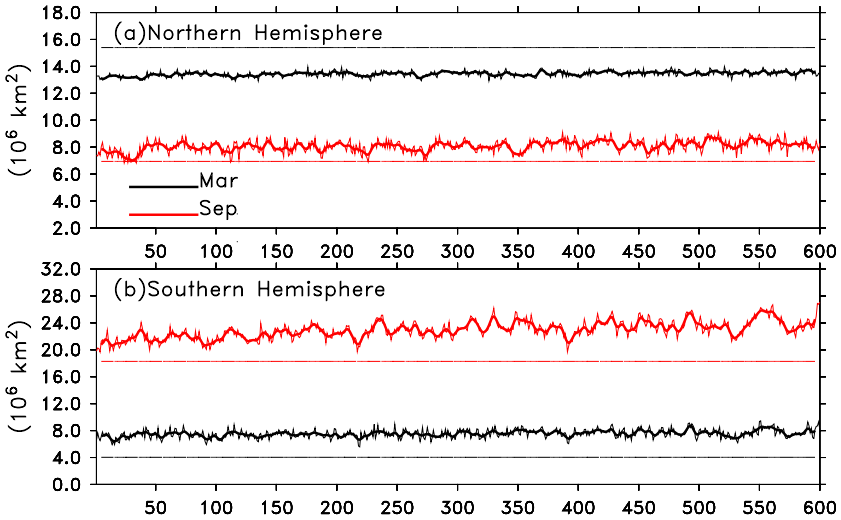

Fig. 3. 600-yr time series of sea ice extents (10^6 km^2) in the NH (a) and in the SH (b) in the preindustrial run simulated by FGOALS-s2. The black and red lines represent March and September, respectively. The thin lines are annual mean values and the thick lines are their 9-yr running mean values. The dashed lines are the observed values from Cavalieri and Parkinson (2003).

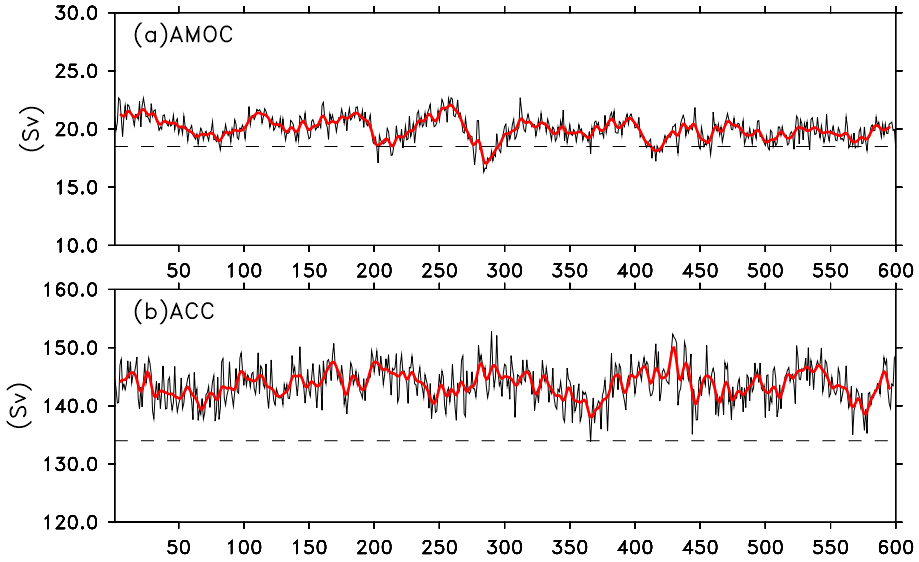

Fig. 4. 600-yr time series of (a) AMOC transport value (Sv; 1 Sv=10^6 m^3 s^{-1}) averaged from 900–1200 m and 25°–35°N; and (b) the depth-integrated volume transport (Sv) through the Drake Passage, defined as the barotropic stream functions at 68.5 W section in the preindustrial run simulated by FGOALS-s2. The black thin lines are annual mean values and the red thick lines are their 9-yr running mean values. The dashed lines in (a) and (b) are the mean observed values from RAPID (Cunningham et al., 2007) and Cunningham et al. (2003), respectively.

AMOC (∼20 Sv) and ACC (∼143.7 Sv) were close to observed values of 18.5 Sv and 135 Sv, which were obtained from RAPID (the UK Natural Environment Research Council's Rapid Climate Change program; Cunningham et al., 2007) and from Cunningham et al. (2003), respectively.

3.2 *Mean climatology*

Figure 5 shows observed SSTs, simulated SSTs and their biases. The areas of the Indo-Pacific warm pool enclosed by a 28°C isotherm in FGOALS-s2 was larger than in FGOALS-s1.0 (Zhou et al., 2005; Bao et al., 2010). This is an important improvement for FGOALS-s2 relative to previous FGOALS versions (Zhou et al., 2005; Bao et al., 2010). This improvement is strongly associated with improvement in meridional wind stress across the equator near the eastern coast of the Pacific Ocean, which may be due to the improved convection, cloud processes and other processes (Bao et al., 2012). At high latitudes, the simulated domains surrounded by the 0°C isotherm were similar to observed domains. This implies that simulated sea ice distributions in the NH and the SH are reasonable (Bao et al., 2012).

However, there were still some obvious biases relative to observation. The large SST biases (exceeding 3°C) were mainly located at SST fronts (i.e. areas where SST experienced a strong gradient) or around the strong western boundary currents (such as the East Australian Current southeast of Australia, the Agulhas Current south of South Africa, the Brazil Current southeast of Argentina, the Gulf Stream, and the connection between the Kuroshio and Oyashio currents) and in the Barents Sea. In the western Pacific pool, cold biases dominated; the areas and the extension enclosed by the 28°C isotherm were much smaller than equivalent observed areas. However, in the stand-alone LICOM2.0, warm biases have been reported in the same regions (Liu et al., 2012). Therefore, the cold biases in FGOALS-s2 may be due to atmospheric processes and air–sea interaction. A cold bias was also seen in the Pacific cold tongue, which is sensitive to surface mixing, the water temperature in the thermocline off the equator, and other factors (e.g. Lin et al., 2008, 2010). Along the eastern coasts of the Pacific and Atlantic Oceans, warm biases were observed both in FGOALS-s2 and in the stand-alone LICOM2.0 forced by wind and flux data (Liu et al., 2012). The warm biases in FGOALS-s2 may be due to biases in low-level atmospheric clouds and the coastal oceanic upwelling related to horizontal resolution. These biases exist in most coupled models (e.g. Mechoso et al., 1995; Davey et al., 2002). Warm biases were also seen in the Northwest Pacific north of 20°N (including along the Kuroshio current and its extension, in the East China Sea and in the Sea of Japan). While

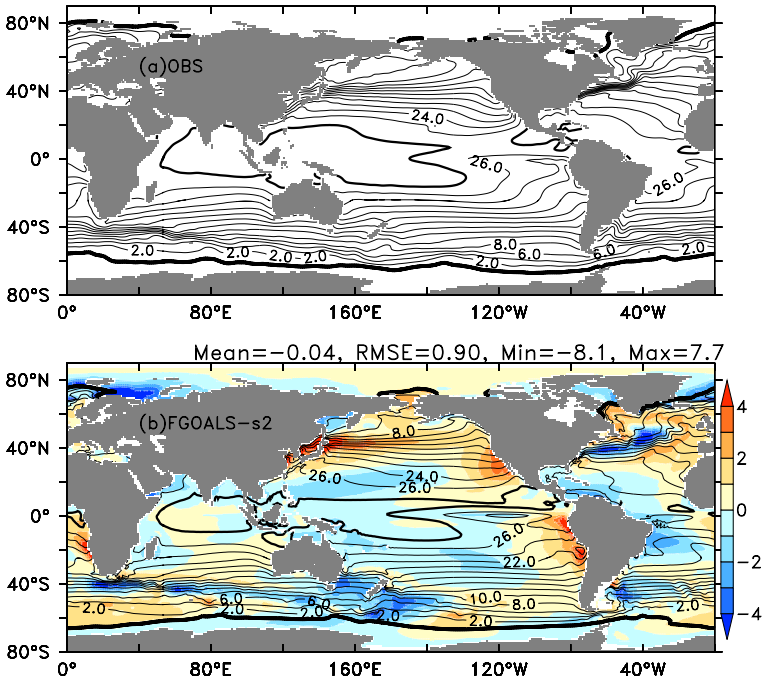

Fig. 5. (a) The observed annual mean SST from ERSST; (b) the simulated SST (contour) and the biases (defined by the difference between simulation minus observation; shaded) in FGOALS-s2. The dark thick lines are for 0°C and 28°C isotherms.

at the same latitude in the Northwest Atlantic, there were cold biases along the Gulf Stream and its extension.

To reveal the origin of the simulated SST biases, the surface net heat fluxes, shortwave radiation and latent heat flux biases are shown in Fig. 6. At oceanic fronts with large cold biases, the ocean obtained greater net heat fluxes relative to observations. Therefore, these cold biases cannot be explained by greater net heat fluxes obtained by the ocean locally. However, in the western Pacific warm pool and around its eastern boundary, net heat fluxes obtained by the ocean were smaller than observations. In this case, the decrease of net heat fluxes would have contributed to the cold biases of SST. In general, shortwave radiation was overestimated in FGOALS-s2 (Fig. 6b), relative to observations. Therefore, the small net heat fluxes obtained by the ocean were mainly due to the changes in latent heat fluxes in FGOALS-s2 (Fig. 6c). Along eastern coasts in the Pacific and Atlantic, incoming shortwave radiation was overestimated by 50 W m^{-2}, which was due to underestimation of low-level clouds. This contributes to the warm biases of SST in FGOALS-s2. Along the Kuroshio current and its extension north of 20°N, the greater number of net heat fluxes obtained from the ocean may contribute to the surface warm biases. However, in the western North Atlantic, the surface cold biases cannot be explained by more net heat fluxes obtained by the ocean.

Figure 7 shows observed SSSs, simulated SSSs and their biases. In the subtropics, the observed SSS was high (Fig. 7a) due to high evaporation (E). In the ITCZ, the observed SSS was low due to heavy precipitation (P; Fig. 7a). The local maximal SSS values were located closer to the eastern coasts in the Pacific and Indian Oceans in FGOALS-s2 than in observations, which was related to low-salinity water located in the western tropical Pacific and Indian Oceans. At these locations, excessively fresh water (corresponding to the negative SSS biases) can be explained by the biases of E minus P, which were in turn mainly due to excessive precipitation in FGOALS-s2 (Figs. 8a and b). However, in the North Atlantic, the seawater was saltier in FGOALS-s2 than in observations, except in the region around 40°N. The salty biases were related to the high evaporation in FGOALS-s2 (Fig. 8c). In addition, at high latitudes in the NH, the large negative SSS biases (exceeding 1.5 psu fresher than observed) were located from 0°–100°E of longitude and positive SSS biases (>1.5 psu saltier than observed) were located between 100°–280°E of longitude. This cannot be simply explained by E minus P and its cause is left for further analysis.

The sea surface is connected with the oceanic deep layer by the upper oceanic boundary layer or mixed layer. The mixed layer depth (MLD) is an important

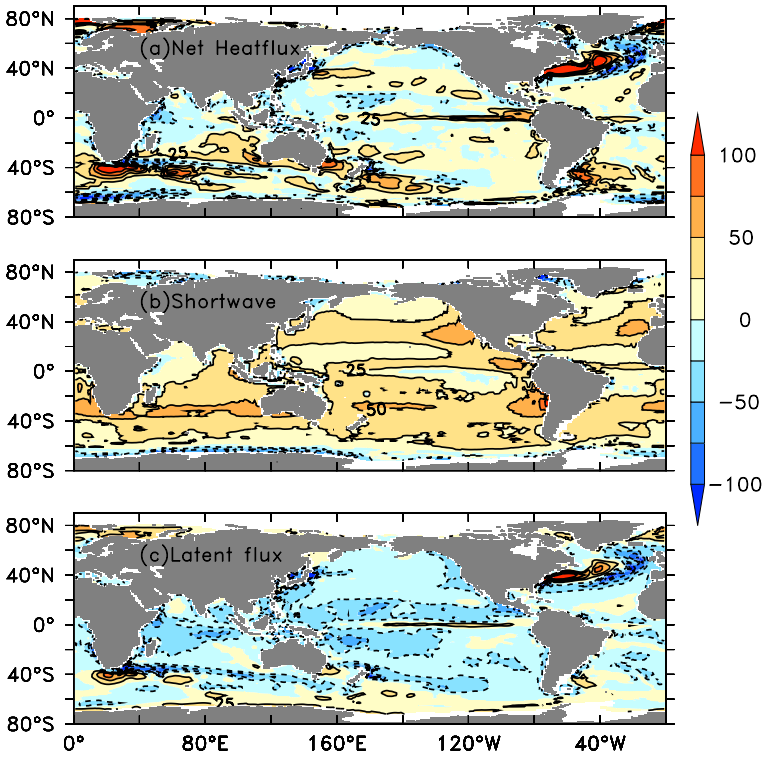

Fig. 6. (a) The simulated biases of net heat fluxes (positive downward); (b) the simulated biases of net shortwave radiation at the sea surface; and (c) the biases of latent heat flux in FGOALS-s2. The thick lines are for 25 and 50 W m^{-2}. The positive value is for heat gain by the ocean. The observed net heat flux, shortwave radiation and latent heat flux are from NOC1.1.

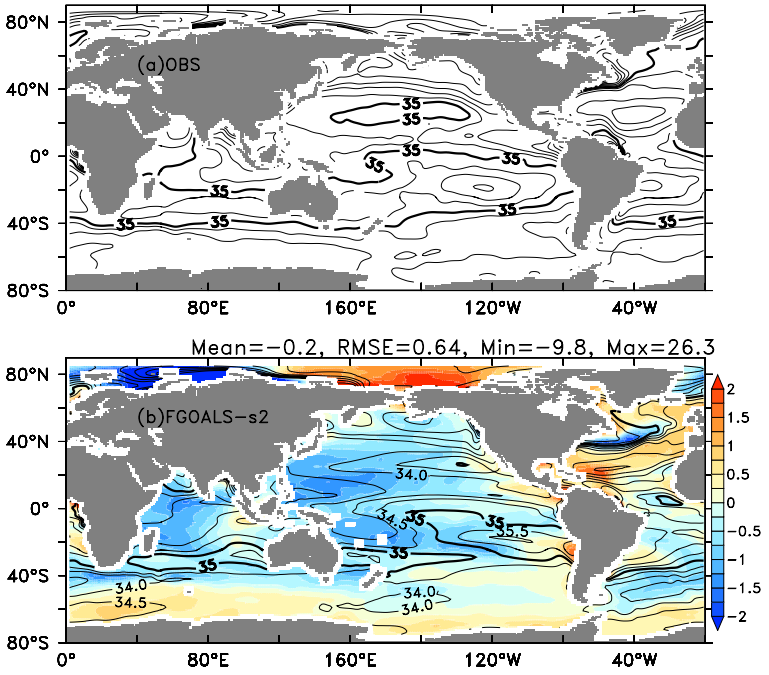

Fig. 7. (a) The observed annual mean SSS from PHC v3.0; (b) the simulated SSS (contour) and the biases (shaded) in FGOALS-s2. The thick line is for 35 psu.

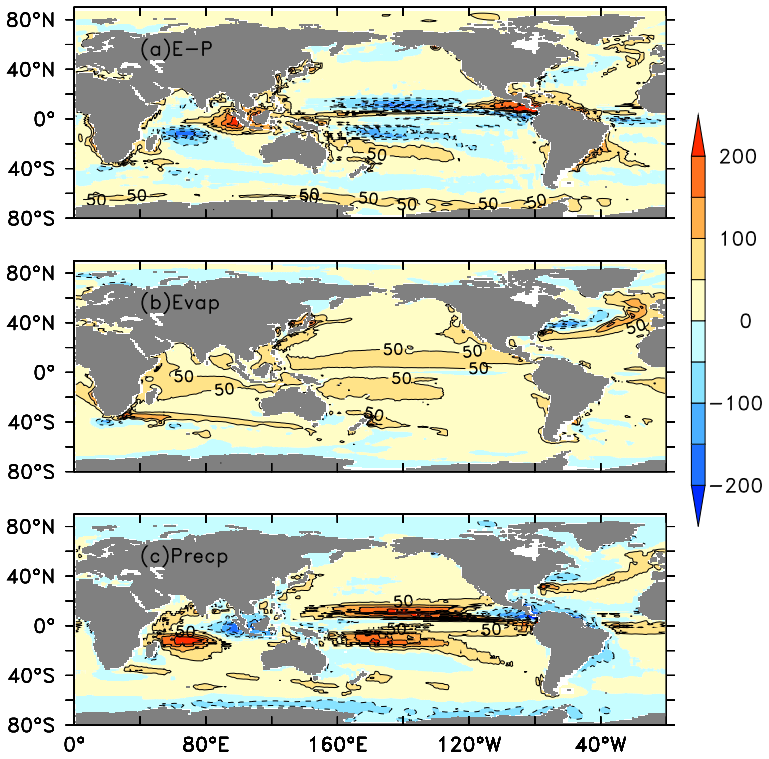

Fig. 8. The simulated biases of (a) E-P (evaporation minus precipitation); (b) evaporation; and (c) precipitation in FGOALS-s2. The contour intervals are for 50 cm yr^{-1}. The observed evaporation and precipitation are from OAFLUX and GPCP, respectively. The positive values of evaporation and precipitation are upward and downward, respectively.

measurement for mixing strength. In the western Pacific and Indian Ocean and in the eastern Pacific and tropical Atlantic, MLDs were shallow in FGOALS-s2 and in observations (Fig. 9). The shallow MLDs in the western Pacific and Indian Ocean may be due to weak stirring related to low wind speeds (Fig. 10). In observations, in the western Indian Ocean, eastern Pacific and Atlantic, the ocean obtained large net heat fluxes and the wind speed was relatively low. The stratifications were relatively stable and MLDs were shallow. The shallow MLDs were better captured in FGOALS-s2 than in FGOALS-s1.0. However, in the South Indian Ocean and the Arabian Sea, the simulated MLDs in FGOALS-s2 were overestimated.

In the middle and high latitudes, due to strong stirring and large losses of turbulent heat fluxes from the ocean related to high wind speed, the simulated MLDs agreed well with observations. Simulated MLDs reached 1000 m in the North Pacific southwest of the Bering Strait, the Southern Ocean, the Labrador Sea, and around Iceland. In the Southern Ocean and the Labrador Sea, simulated MLDs were overestimated. Between 20°–45°N of latitude, FGOALS-s2 also overestimated the MLD.

The simulated basic vertical structure of ocean temperature in FGOALS-s2 was almost consistent with observations; for instance, uplift of isotherms in the tropics and sinking in the middle latitudes (Fig. 11). In FGOALS-s2, the structures of the biases can be divided into five different layers: warm biases in the tropical thermocline; cold biases at the surface, in the deep layer around 2500 m, in the permanent thermocline, and at the ocean bottom. The cold biases south of 45°S are connected with the cold biases in the deep layer around 2500 m. The warm anomalies in the tropical thermocline around 20°N are associated with the overestimated MLDs in the north Pacific and Atlantic Ocean. The warmest biases (exceeding 4°C) occurred below 600 m north of 65°N in the NH. Warm biases also exist in the stand-alone LICOM2.0, but with small magnitudes (Liu et al., 2012). The warm biases in FGOALS-s2 may be related to strong mixing north of 60°N (Fig. 9).

The structure of zonal mean salinity (Fig. 11) can be used as an indicator of water mass. In observations, around 50°S, there was a region of low salinity mass called the Antarctic Intermediate Water (AAIW). The main feature of AAIW is a tongue of low salinity, sink-

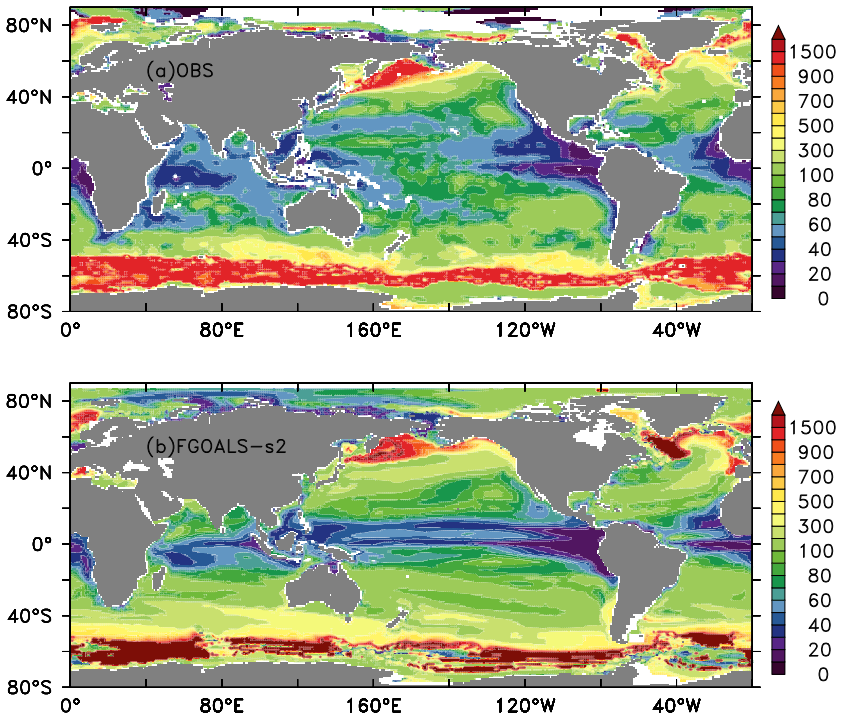

Fig. 9. The maximum MLD (m) for the climatology of (a) observation from WOA05 (Locarnini et al., 2006); and (b) FGOALS-s2. The MLD is defined as the depth where temperature change compared to temperature at 10 m.

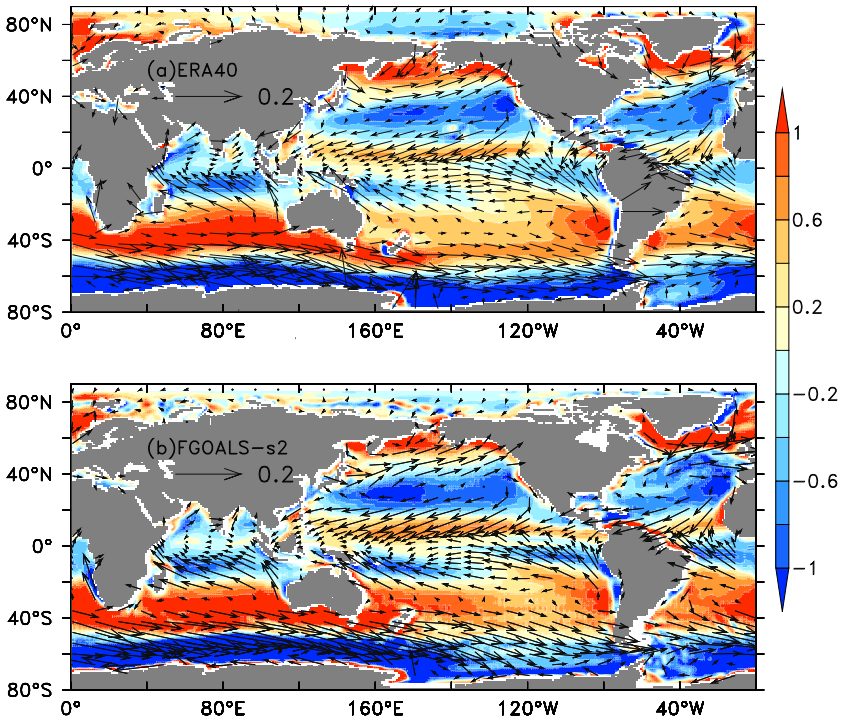

Fig. 10. (a) The wind stress (N m^{-2}) and its curl (10^{-7} N m^{-3}) from ERA40; and (b) the simulated wind stress and its curl by FGOALS-s2.

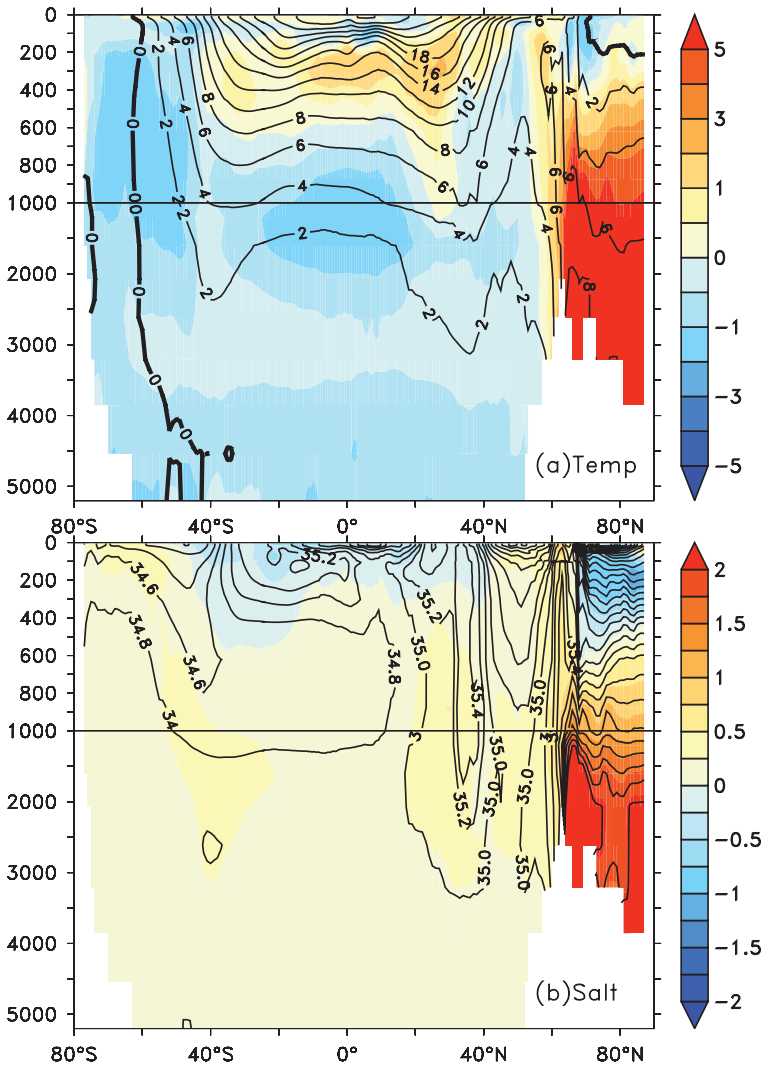

Fig. 11. (a) The simulated zonal mean temperatures (contour; °C) and the biases (shaded); (b) the same as (a) but for salinity (psu) in FGOALS-s2. The observed temperatures and salinities are from PHC3.0. The y-axis is water depth (m) and the x-axis is the latitude.

ing from the surface to 1200 m and extending northward at depth to the equator. FGOALS-s2 captured effectively the observed features of AAIW. The improvement in the simulation of AAIW can be traced to oceanic internal processes. Between 40°S–40°N, the salinity biases presented in a three-layer structure, top-down: the layers above the 500-m layer and below the 4000-m layer had freshwater biases, while the deep layer between 500 m and 4000 m had a salty bias. South of 40°S, the seawater had a salty bias in the upper 300 m, which was connected to the biases around 2500 m from 60°S–60°N. Between 40°–60°N, there were salty biases in the whole layer. The biases were mainly located in the North Atlantic, due to high evaporation. North of 65°N, there was a freshwater bias above 600 m and a salty bias (exceeding 1.5 psu) below 600 m. Similar to the warmest biases, the saltiest biases were limited to just those regions north of 65°N.

To clearly show the large-scale circulations directly simulated by FGOALS-s2, the barotropic stream functions (BSFs) are depicted in Fig. 12. There were anticyclonic circulations (i.e. subtropical gyres) driven by negative wind stress curls (Fig. 10) including two major boundary currents in the NH, Kuroshio current and Gulf Stream. The simulated maximal transport of the Kuroshio current was about 36.4 Sv at 21.5°N and 38 Sv at 23°N; these values were close to observed and theoretical values (Yuan et al., 1998; Lee et al., 2001). However, the maximal transport of the Gulf Stream was about 39.5 Sv (at 27°N), which was larger than the observed value (∼32 Sv; Leaman et al., 1987). More-

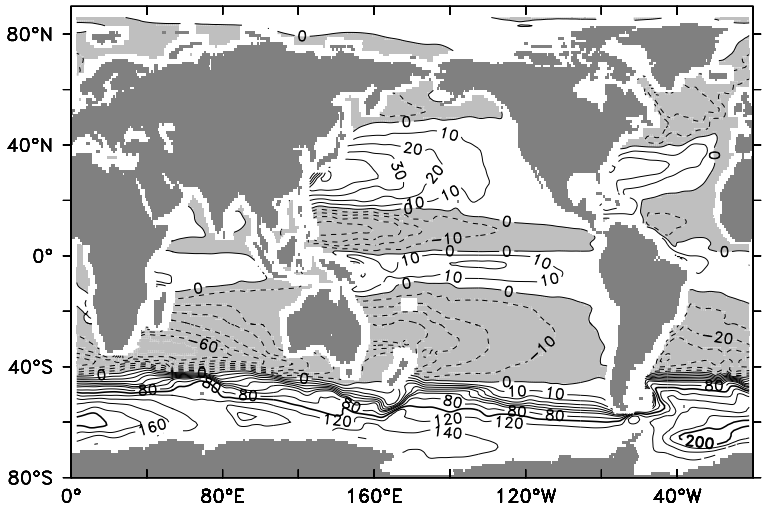

Fig. 12. The simulated BSFs (Sv) by FGOALS-s2. The thick lines are for 100 and 200 Sv. The cyclonic circulations are shaded gray.

over, the position of maximal transport at 27°N was located at 76°W and deviated farther away from the western boundary (by 3° longitude) than the observed value (79.5°W; Leaman et al., 1987). In the Pacific, north of 40°N, the subpolar gyre was about 10 Sv, which was close to the observational value (Wunsch, 2011). In the North Atlantic, the subpolar gyre was about 30 Sv (observed estimates range from 25–40 Sv; e.g. Clarke, 1984; Bacon, 1997). The subpolar gyres were caused by positive wind curl (Fig. 10).

One of the most obvious oceanic currents, the ACC is located in the Southern Ocean. The maximal transport of the ACC can reach 200 Sv in the Weddell Sea. The transport through the Drake Passage was about 140 Sv in FGOALS-s2, which was comparable with an observation of 135 Sv (Cunningham et al., 2003). The simulated ACC in FGOALS-s2 is greatly improved relative to that in FGOALS-s1.0 (Zhou et al., 2005). The improvement in FGOALS-s2 will be further analyzed and clarified.

FGOALS-s2 was found to accurately simulate trade winds in the tropical Pacific and Atlantic, the cross-equatorial flows in the Indian Ocean and eastern Pacific, and the magnitude and position of westerly wind belts (Fig. 10). Simulations agreed closely with with values from ERA40, a climate database managed by the European Centre for Medium-Range Weather Forecasts (Fig. 10). Due to the reasonable wind stresses, the derived vorticities in FGOALS-s2 agreed well with those derived from ERA40 (Fig. 10; shaded). According to classic Sverdrup theories, the credible wind stresses and their derived vorticities drive reasonable large-scale ocean circulations in FGOALS-s2 (Fig. 12).

Ocean meridional circulations play an important role in transporting heat. Figure 13 shows the global meridional overturning circulation (MOC) and AMOC. FGOALS-s2 achieved high accuracy in simulating tropics–subtropics cells in the upper 500 m, the Deacon cells from the surface to 3500 m (∼36 Sv), the North Atlantic Deep Water (NADW) between 800–2500 m north of 35°S, and the Antarctic Bottom Water (AABW) below 3000 m. These agreed well with observed values (Lumpkin and Speer, 2007) and other simulation values (e.g. Meehl et al., 2007; Kuhlbrodt et al., 2007). The observed maximal transport magnitude of NADW at 26.5°N is about 18.5 Sv according to RAPID and the simulation value was about 19 Sv (Fig. 13c). The depth of the maximal magnitude simulated by FGOALS-s2 was 1000 m, which agreed with observations. The simulated transport of AABW south of 35°S was 12–16 Sv, which was also consistent with observations (Lumpkin and Speer, 2007). At 26.5°N, the simulated AABW transport was larger than the observed transport (Fig. 13c).

The meridional circulations carry surface warm water poleward and cool water at depth equatorward. Values for the meridional heat transport (MHT) in the global ocean, Atlantic and Indo-Pacific Ocean are presented in Fig. 14. Globally, heat is transported from the equator to high latitudes. The maximal MHT was located at 22°N with a magnitude of 1.8 PW, which was close to observations made by Ganachaud and Wunsch (2003). At 45°N, the northward MHT in FGOALS-s2 was larger than observations. However, at 20°S and 30°S, the southward MHTs were smaller than observations. In the Atlantic, the observed and simulated MHTs were transported northward, north of 35°S. However, the simulated MHTs were smaller than observed MHTs south of 30°N and larger than

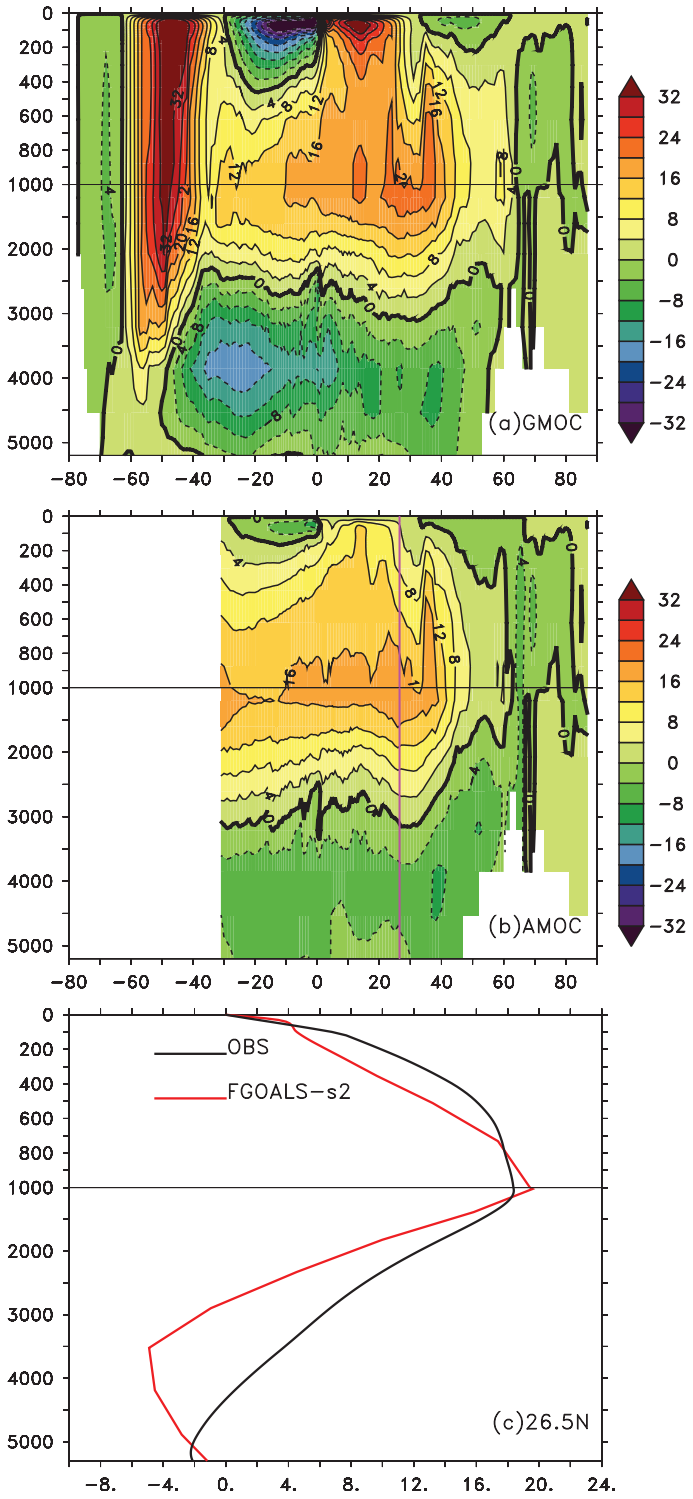

Fig. 13. (a) The simulated MOC (Sv) and (b) AMOC in FGOALS-s2. The contour interval is 4 Sv. (c) The AMOC (Sv) at 26.5°N, which is indicated by the purple red line in (b). The observed value is the mean value between 2004–09. The y-axis is water depth (m). The x-axis is the latitude in (a) and (b), while the x-axis in (c) is the AMOC values (Sv).

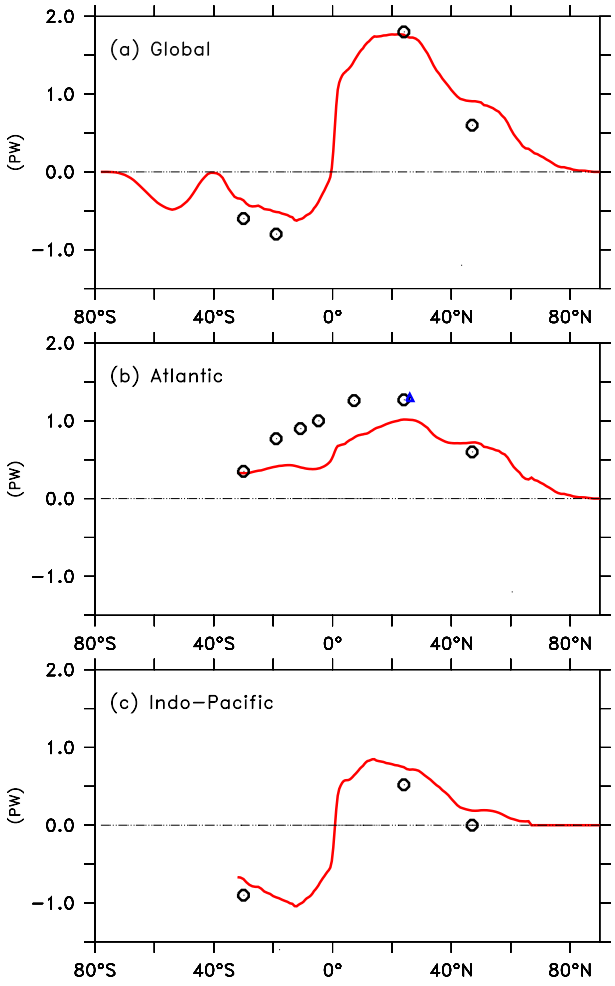

Fig. 14. (a) Global, (b) Atlantic and (c) Indo-Pacific meridional or polarward heat transport (1 PW=10^{15} W) for FGOALS-s2 (red solid line). The black dots are estimations from Ganachaud and Wunsch (2003). The blue triangle at 26.5°N is the estimation from RAPID.

observed north of 40°N (Ganachaud and Wunsch, 2003). The weaker northward MHTs also exist in most other models (Large and Danabasoglu, 2006). At 26°N, the simulated MHT in FGOALS-s2 was 1 PW, smaller than that observed in RAPID (Cunningham et al., 2007).

4. Summary and discussion

Forced by preindustrial solar radiation and greenhouse gases (i.e. fixed external forcing), FGOALS-s2 was integrated successfully for thousands of model years without obvious climate drift, as verified by examining the global mean thermal and hydro fields and ocean circulations. During a 600-year period, the linear trends of SST and SSS were -0.04°C (100 yr)$^{-1}$ and 0.01 psu (100 yr)$^{-1}$, respectively. Meanwhile, the linear trends of the strength of AMOC and the transport of ACC were -0.18 Sv (100 yr)$^{-1}$ and 0.02 Sv (100 yr)$^{-1}$, respectively. For sea ice extent, the linear trend in September in the SH was relatively large [$\sim 0.47\times10^6$ km^2 (100 yr)$^{-1}$], larger than that [$\sim 0.09\times10^6$ km^2 (100 yr)$^{-1}$] in the NH. Furthermore, in the preindustrial run, the sea surface lost net heat flux and water flux, which caused a decrease in global volume-mean ocean temperatures and an increase in global volume-mean ocean salinity, respectively.

By comparing the simulation results with observational data, several important improvements were revealed. First, the simulated SSTs have become warmer and the area of the warm pool in the tropics has increased obviously relative to previous FGOALS-s versions (1.0 and 1.1). The related MLD, wind stress and wind stress curls have become more reasonable. Second, the temperature and salinity structures have improved, except for deep layers at high latitudes in the NH. The AAIW is well simulated by FGOALS-s2 as a result of the improvement of the stand-alone LICOM2.0. Third, the magnitudes of Kuroshio transport, AMOC and ACC at the Drake Passage are now much closer to observed values than in FGOALS-s1.0. In addition, the simulated global meridional heat transport and associated sea ice distributions are closer to observations in FGOALS-s2.

Although there are improvements in FGOALS-s2, some common biases were still found to exist, as is the case for most state-of-the-art coupled models. Biases in FGOALS-s2 were found to include a cold bias in the eastern Pacific cold tongue, as well as its westward extension; plus, a warm bias along eastern coasts in the Pacific and Atlantic Ocean. The warm bias was found mainly to be due to the overestimation of shortwave radiation resulting from an underestimation of low-level clouds and the weak oceanic coastal upwelling due to the coarse resolution of the AGCM and OGCM. In the tropics, the extension of the western Pacific warm pool was found to still be small and shallow compared to observation. The excessive loss of net heat flux from the ocean contributes to this bias. Large SST biases (exceeding 3°C) were found to be located in areas of observed SST fronts, or around strong western boundary currents. Local net heat fluxes do not contribute to the cold biases, which instead may be attributable to unresolved mesoscale processes due to the coarse horizontal resolution of the OGCM and AGCM (Yu et al., 2012).

In the western Pacific and Indian Ocean, a surface freshwater bias was found to be mainly due to excessively heavy precipitation. The precipitation bias also then leads to a freshwater bias in the vertical dimen-

sion. In the North Atlantic, the salty bias was found to be due to high evaporation. In the Arctic Ocean, the large SSS biases (exceeding 1.5 psu) cannot be explained by E minus P, and may instead be related to the dynamical processes of sea ice.

Different surface biases were found to exist around the Kuroshio current and the Gulf Stream. Two factors may contribute to the warm biases around Kuroshio. The first is large MHT in the Indo-Pacific basin relative to the observed value (Fig. 14c). Such a large MHT would lead to the accumulation of heat, warming the SST in the Pacific basin. Furthermore, a greater number of net heat fluxes obtained by the ocean may also contribute to the warm biases. In FGOALS-s2, around the Gulf Stream it was found to be mainly dominated by cold biases, which were related to weak MHT in the Atlantic (Fig. 14b). Such weak transport may be due to oceanic dynamical processes, vertical mixing and a coarse horizontal resolution.

Biases of temperature and salinity were also found to exist in the vertical dimension, with maximums located below 600 m in depth, north of 60°N in the NH, and values exceeding 4°C and 2 psu, respectively. These biases may be caused by large diffusion coefficients, which mix the warm and salty water to deep layers where it can accumulate. The problem arises because the North Pole, unlike the South Pole, exists over ocean, and thus must be simulated by the model; however, as the longitude lines converge at the pole, the model grid and time-step must both decrease. To preserve model stability and avoid time steps that are too small, the OGCM uses zonal filters to smooth the unstable signal. This will act to reduce the mixing; however, it may cause the coupled model to drift gradually due to the reduction in the strength of AMOC. Therefore, large diffusion coefficients are used to maintain long-term integrations. To use proper mixing and make the high-latitude filter unnecessary in future versions of LICOM, the North Pole needs to be redefined in the future to place it over a land mass, as is done in other OGCMs, such as the Parallel Ocean Program (POP) or Modular Ocean Model version 4 (MOM4).

In conclusion, this version of FGOALS demonstrates some significant improvements relative to previous versions (FGOALS-s1.0 and FGOALS-s1.1). These improvements include more accurate simulations of AMOC and ACC and AAIW, among other features. In addition, FGOALS-s2 can better capture the seasonal cycle of equatorial SST and ENSO. These improvements and the existence of large biases need to be evaluated in detail, and their causes and effects need to be clarified one-by-one in future. This is a goal for future work.

Acknowledgements. We wish to thank the two anonymous reviewers for their very valuable comments that helped to improve our paper. We acknowledge ZHOU Tianjun—Director of the LASG model development group—and the support received from the whole LASG department. In particular, we would like to thank ZHANG Xuehong for his attention and comments; BAO Qing for providing the data; and SONG Zhenya, ZHAO Wei , GUO Zhun, LIU Jiping, SONG Mirong HE Jie, and HE Bian for their kind help. The authors are supported by the National Key Program for Developing Basic Sciences (Grant Nos. 2010CB950502), the "Strategic Priority Research Program—Climate Change: Carbon Budget and Related Issues" of the Chinese Academy of Sciences (Grant No. XDA05110302), the National Natural Science Foundation of China (Grant Nos. 40906012 and 41023002), and National High Technology Research and Development Program of China (Grant No. 2010AA012303).

REFERENCES

Adler, R. F., and Coauthors, 2003: The Version 2 Global Precipitation Climatology Project (GPCP) Monthly Precipitation Analysis (1979–Present). *J. Hydrometeorology*, **4**, 1147–1167.

Antonov, J. I., R. A. Locarnini, T. P. Boyer, A. V. Mishonov, and H. E. Garcia, 2006: *Salinity.* Vol. 2, *World Ocean Atlas 2005*, S. Levitus, Ed., NOAA Atlas NESDIS 62, U.S. Government Printing Office, Washington, D. C., 182pp.

Bacon, S. 1997: Circulation and Fluxes in the North Atlantic between Greenland and Ireland. *J. Phys. Oceanogr.*, **27**, 1420–1435.

Bao, Q., G. X. Wu, Y. M. Liu, J. Yang, Z. Z. Wang, and T. J. Zhou, 2010: An Introduction to the Coupled Model FGOALS1.1-s and Its Performance in East Asia, *Adv. Atmos. Sci.*, **27**(5), 1131–1142, doi: 10.1007/s00376-010-9177-1.

Bao, Q., and Coauthors, 2012: The Flexible Global Ocean-Atmosphere-Land System model Version: FGOALS-s2. *Adv. Atmos. Sci.*. (in press)

Canuto, V. M., A. Howard, Y. Cheng, and M. S. Dubovikov, 2001: Ocean turbulence. Part I: One-point closure model—Momentum and heat vertical diffusivities. *J. Phys. Oceanogr.*, **31**, 1413–1426.

Canuto, V. M., A. Howard, Y. Cheng, and M. S. Dubovikov, 2002: Ocean turbulence. Part II: Vertical diffusivities of momentum, heat, salt, mass, and passive scalars. *J. Phys. Oceanogr.*, **32**, 240–264.

Cavalieri, D. J., and C. L. Parkinson, 2003: 30-year satellite record reveals contrasting Arctic and Antarctic decadal sea ice variability. *Geophys. Res. Lett.*, **30**(18), doi: 10.1029/2003GL018031.

Chen, K. M., X. H. Zhang, and X. Z Jin, 1997a: A coupled ocean-atmosphere general circulation model for studies of global climate change. I. Formulation and performance of the model. *Acta Oceanologia Sinica*,

19(3), 21–32. (in Chinese)

Chen, K. M., X. H. Zhang, X. Z Jin, Y. Q. Yu, and Y. F. Guo, 1997b: A coupled ocean-atmosphere general circulation model for studies of global climate changes: II. Preliminary analyses on climate drift and enhanced greenhouse effect. *Acta Oceanologia Sinica*, **19**(4), 26–40. (in Chinese)

Chen, Q. Y., Y. Q. Yu, Y. F. Guo, and X. H. Zhang, 1996: Climatic change in East Asia induced by greenhouse effect. *Climatic and Environmental Research*, **1**, 113–123. (in Chinese)

Clarke, R. A., 1984: Transport through the Cape Farewell-Flemish Cap section. *Rapports et Proces-Verbaux. Reun. Cons. int. Explor. Mer*, **185**, 120–130. (in French)

Cunningham, S. A., S. G. Alderson, B. A. King, and M. A. Brandon, 2003: Transport and variability of the Antarctic Circumpolar Current in Drake Passage. *J. Geophys. Res.*, **108**, 8084, doi: 10.1029/2001JC001147.

Cunningham, S. A., and Coauthors, 2007: Temporal variability of the Atlantic Meridional Overturning Circulation at 26°N. *Science*, **317**, 935–938, doi: 10.1126/science.1141304.

Davey, M. K., and Coauthors, 2002: STOIC: A study of coupled model climatology and variability in tropical ocean regions. *Climate Dyn.*, **18**, 403–420.

Ganachaud, A., and C. Wunsch, 2003: Large-scale ocean heat and freshwater transports during the World Ocean Circulation Experiment. *J. Climate*, **16**, 696–705.

Gent, P. R., and J. C. McWilliams, 1990: Isopycnal mixing in ocean circulation models. *J. Phys. Oceanogr.*, **20**, 150–155.

Grist, J. P., and S. A. Josey, 2003: Inverse analysis adjustment of the SOC air-sea flux climatology using ocean heat transport constraints. *J. Climate*, **20**, 3274–3295, doi: http://dx.doi.org/10.1175/1520-0442(2003)016<3274:IAAOTS>2.0.CO;2.

Jin, X. Z., X. H. Zhang, and T. J. Zhou, 1999: Fundamental framework and experiments of the third generation of IAP/LASG world ocean general circulation model. *Adv. Atmos. Sci.*, **16**, 197–215.

Kuhlbrodt, T., A. Griesel, M. Montoya, A. Levermann, M. Hofmann, and S. Rahmstorf, 2007: On the driving processes of the Atlantic meridional overturning circulation. *Rev. Geophys.*, **45**, RG2001, doi: 10.1029/2004RG000166.

Large, W. G., and G. Danabasoglu, 2006: Attribution and impacts of upper-ocean biase in CCSM3. *J. Climate*, **19**, 2325–2346.

Leaman, K. D., R. L. Molinari, and P. S. Vertes, 1987: Structure and variability of the Florida Current at 27°N: April 1982–July 1984. *J. Phys. Oceanogr.*, **17**, 565–583.

Lee, T. N., W. E. Johns, C. T. Liu, D. Zhand, R. Zantopp, and Y. Yang, 2001: Mean transport and seasonal cycle of the Kuroshio east of Taiwan with comparison to the Florida Current. *J. Geophys. Res.*, **106**, 22143–22158.

Lin, P. F., H. L. Liu, and X. H. Zhang, 2007: Sensitivity of the upper ocean temperature and circulation in the equatorial Pacific to solar radiation penetration due to phytoplankton. *Adv. Atmos. Sci.*, **24**(5), 765–780, doi: 10.1007/s00376-007-0765-7.

Lin, P. F., H. L. Liu, and X. H. Zhang, 2008: Effect of chlorophyll-a horizontal distribution on upper ocean temperature in the central and eastern equatorial Pacific. *Adv. Atmos. Sci.*, **25**(4), 585–596, doi: 10.1007/s00376-008-0585-4.

Lin, P. F., H. L. Liu, C. Li, and X. H. Zhang, 2010: Spring cold bias of SST and minimal wind mixing in the equatorial Pacific cold tongue. *Atmos. Oceanic Sci. Lett.*, **3**, 342–346.

Lin, P. F., H. L. Liu, Y. Q. Yu, and X. H. Zhang, 2011: Response of Sea surface temperature to chlorophyll-a concentration in the tropical Pacific: Annual mean, seasonal cycle and interannual variability. *Adv. Atmos. Sci.*, **28**(3), 492–510, doi: 10.1007/s00376-010-0015-2.

Liu, H. L., X. H. Zhang, W. Li, Y. Q. Yu, and R. C. Yu, 2004a: A eddy-permitting oceanic general circulation model and its preliminary evaluations. *Adv. Atmos. Sci.*, **21**, 675–690.

Liu, H. L., Y. Q. Yu, W. Li, and X. H. Zhang, 2004b: *Manual for LASG/IAP Climate System Ocean Model* (*LICOM1.0*). Science Press, Beijing, 1–128. (in Chinese)

Liu, H. L., P. F. Lin, Y. Q. Yu, and X. H. Zhang, 2012: The baseline evaluation of LASG/IAP Climate system Ocean Model (LICOM) version 2.0. *Acta Meteorologica Sinica*, **26**(3), 318–329.

Locarnini, R. A., A. V. Mishonov, J. I. Antonov, T. P. Boyer, and H. E. Garcia, 2006: *Temperature. Vol.1, World Ocean Atlas 2005*, S. Levitus, Ed., NOAA Atlas NESDIS 61, U. S. Government Printing Office, Washington D.C., 182pp.

Lumpkin, R., and K. Speer, 2007: Global ocean meridional overturning. *J. Phys. Oceanogr.*, **37**, 2550–2562.

Mechoso, C., and Coauthors, 1995: The seasonal cycle over the tropical Pacific in coupled ocean–atmosphere general circulation models. *Mon. Wea. Rev.*, **123**, 2825–2838.

Meehl, G. A., and Coauthors, 2007: Global climate projections. *Climate Change 2007: The Physical Science Basis. Contribution of Working Group I to the Fourth Assessment Report of the Intergovernmental Panel on Climate Change*. S. Solomon et al., Eds., Cambridge University Press, Cambridge, United Kingdom and New York, New York, 996pp.

Ohlmann, J., 2003: Ocean radiant heating in climate models. *J. Climate*, **16**, 1337–1351.

Pacanowski, R., and S. Philander, 1981: Parameterization of vertical mixing in numerical models of tropical oceans. *J. Phys. Oceanogr.*, **11**, 1443–1451.

Smith, T. M., R. W. Reynolds, T. C. Peterson, and J. Lawrimore, 2008: Improvements to NOAA's Histori-

cal Merged Land–Ocean Surface Temperature Analysis (1880–2006). *J. Climate*, **21**, 2283–2296.

Steele, M., R. Morley, and W. Ermold, 2001: PHC: A global ocean hydrography with a high quality Arctic Ocean. *J. Climate*, **14**, 2079–2087.

Uppala, S., and Coauthors, 2005: The ERA-40 reanalysis. *Quart. J. Roy. Meteor. Soc.*, **131**, 2961–3012.

Wu, F. H., H. L. Liu, W. Li, and X. H. Zhang, 2005: Effect of adjusting vertical resolution on the eastern equatorial Pacific cold tongue. *Acta Oceanologica Sinica*, **24**(3), 1–12.

Wunsch, C., 2011: The decadal mean ocean circulation and Sverdrup balance. *J. Mar. Res.*, **69**, 417–434.

Xiao, C., 2006: Adoption of a two-step shape-preserving advection scheme in an OGCM and its coupled experiment. M.S. thesis, Institute of Atmospheric Physics, Chinese Academy of Sciences, 89pp. (in Chinese)

Xie, P., J. E. Janowiak, P. A. Arkin, R. F. Adler, A. Gruber, R. R. Ferraro, G. J. Huffman, and S. Curtis, 2003: GPCP pentad precipitation analyses: An experimental dataset based on gauge observations and satellite estimates. *J. Climate*, **16**, 2197–2214.

Xue, Y., T. M. Smith, and R. W. Reynolds, 2003: Interdecadal changes of 30-yr SST normals during 1871–2000. *J. Climate*, **16**, 1601–1612.

Yu, L., 2007: Global variations in oceanic evaporation (1958–2005): The role of the changing wind speed. *J. Climate*, **20**(21), 5376–5390.

Yu, L., X. Jin, and R. A. Weller, 2008: Multidecade global flux datasets from the Objectively Analyzed Air-sea Fluxes (OAFlux) Project: Latent and sensible heat fluxes, ocean evaporation, and related surface meteorological variables. OAFlux Project Tech. Rep. OA-2008-01, Woods Hole Oceanographic Institution, Woods Hole, Massachusetts, 64pp.

Yu, Y. Q., R. C. Yu, X. H. Zhang, and H. L. Liu, 2002: A flexible global coupled climate model. *Adv. Atmos. Sci.*, **19**, 169–190.

Yu, Y. Q., X. H. Zhang, and Y. F. Guo, 2004: Global coupled ocean-atmosphere general circulation models in LASG/IAP. *Adv. Atmos. Sci.*, **21**, 444–455.

Yu, Y. Q., W. P. Zheng, X. H. Zhang, and H. L. Liu, 2007: LASG coupled climate system model FGCM-1.0. *Chinese Journal of Geophysics*, **50**(6), 1677–1687. (in Chinese)

Yu, Y. Q., W. P. Zheng, B. Wang, H. L. Liu, and J. P. Liu, 2011: Versions g1.0 and g1.1 of the LASG/IAP Flexible Global Ocean-Atmosphere-Land System Model. *Adv. Atmos. Sci.*, **28**(1), 99–117, doi: 10.1007/s00376-010-9112-5.

Yu, Y. Q., H. L. Liu, and P. F. Lin, 2012: A quasi-global (1/10)° eddy-resolving ocean general circulation model and its preliminary results. *Chinese Science Bulletin*, **57**, 3908–3916, doi: 10.1007/s11434-012-5234-8.

Yuan, Y., A. Kaneko, J. Su, X. Ahu, Y. Liu, N. Gohda, and H. Chen, 1998: The Kuroshio east of Taiwan and in the East China Sea and the currents east of Ryukyu Islands during early summer of 1996. *Journal of Oceanography*, **54**, 217–226.

Zhang, L. X., T. J. Zhou, B. Wu, and Q. Bao, 2010: The annual modes of tropical precipitation simulated by the LASG/IAP coupled ocean-atmosphere model FGOALS_s1.1. *Acta Meteorologica Sinica*, **24**(2), 189–202.

Zhang, X. H., and X. Liang, 1989: A numerical world ocean general circulation model. *Adv. Atmos. Sci.*, **6**, 43–61.

Zhang, X. H., N. Bao, R. C. Yu, and W. Q. Wang, 1992: Coupling scheme experiments based on an atmospheric and an oceanic GCM. *Chinese Journal of Atmospheric Science*, **16**(2), 129–144. (in Chinese)

Zhou, T. J., and Coauthors, 2005: The climate system model FGOALS-s using LASG/IAP spectral AGCM SAMIL as its Atmospheric component. *Acta Meteorologica Sinica*, **63**, 702–715. (in Chinese)